machines

MDPI

Article

Multi-Objective Crashworthiness Optimization of Variable-Thickness Expansion Tubes Using Machine Learning and Decision-Making

Dezhuang Yu [1,2], Haitao Dong [1], Zhanyu Liu [1], Weiyuan Guan [2] and Jijian Lu [2,*]

[1] CRRC Dalian Locomotive and Rolling Stock Co., Ltd., Dalian 116000, China; 13478948866@163.com (D.Y.); 013500016448@crrcgc.cc (H.D.); andy_dht@163.com (Z.L.)
[2] School of Traffic and Transportation Engineering, Central South University, Changsha 410075, China; wy_guan@csu.edu.cn
* Correspondence: lujijian@csu.edu.cn

Abstract

While traditional expansion tubes exhibit excellent energy absorption, their uniform wall thickness limits lightweighting and performance optimization. Graded thickness designs can reduce the initial peak crushing force (*IPCF*) and enhance material efficiency. This paper proposes a variable-thickness expansion tube integrating high energy absorption with tailored mechanical response. Material tensile tests were conducted to determine the constitutive relationship, and axial compression experiments on expansion tubes were performed. Numerical simulations were validated against experimental results, establishing an accurate finite element model. The influence of design parameters on crashworthiness indicators was analyzed via orthogonal experiments. A fully connected neural network with a feature importance layer was then constructed to efficiently replace computationally expensive simulations. Key performance indicators—including *IPCF*, total energy absorption (*EA*), and structural mass (*m*)—were synergistically optimized using a multi-objective genetic algorithm. Finally, the entropy weight–gray relation–TOPSIS method was employed to select the most satisfactory solution from the Pareto front. The relative discrepancies between the selected solution and finite element simulations are 3.65% for *EA*, 0.23% for mass, and 4.37% for *IPCF*, confirming the framework's reliability. This study establishes a systematic design approach combining machine learning, multi-objective optimization, and multi-criteria decision-making for high-performance energy-absorbing structures.

Keywords: variable-thickness expansion tube (VTET); fully connected network with feature importance (FI-FCN); multi-objective optimization; entropy weight–grey relational analysis–TOPSIS (EW-GRA-TOPSIS)

Check for updates

Academic Editor: Yucheng Liu

Received: 16 May 2026
Revised: 7 June 2026
Accepted: 11 June 2026
Published: 16 June 2026

Copyright: © 2026 by the authors. Licensee MDPI, Basel, Switzerland. This article is an open access article distributed under the terms and conditions of the Creative Commons Attribution (CC BY) license.

1. Introduction

Although the widespread application of intelligent control systems and high-precision sensors has significantly reduced the risk of train collisions, accidents remain difficult to completely avoid due to human error, unexpected failures, and extreme environmental conditions [1,2]. Given the high operating speeds and large passenger capacities of modern trains, collisions often result in severe casualties and substantial economic losses. Therefore, improving crashworthiness has become a critical aspect of railway vehicle safety design [3], and the corresponding structural designs must comply with safety standards from

multiple countries [4–6]. In this context, passive safety technologies centered on energy-absorbing structures have attracted increasing attention. Structural optimization for efficient energy absorption and dissipation, while ensuring occupant protection, has become a key focus in crashworthiness research within the rail transit field.

Over the past two decades, the mechanical behavior and energy absorption characteristics of expansion tubes have become a focal point in the field of lightweight protective structures [7–10]. In terms of theoretical modeling, Yan et al. derived an analytical expression for the steady-state force during the expansion deformation of thin-walled tubes, providing a theoretical framework for studying the deformation mechanism [11]. Shakeri et al. achieved accurate prediction of local buckling loads through a modified Plantema equation [12]. Lucanin et al. revealed the mechanical response characteristics of such tubes under different loading rates through quasi-static and dynamic experiments [13]. Choi et al. investigated the effect of impact velocity on energy absorption performance and utilized inverse analysis to determine the friction coefficients under dynamic loading conditions [14]. Yang et al. studied 5A06 aluminum alloy expansion tubes and clarified the effects of wall thickness and die cone angle on load-bearing capacity [15].

Variable-thickness thin-walled structures have attracted widespread attention due to their advantages in lightweight design, high specific strength, and excellent energy absorption capabilities [16–23]. Sun et al. demonstrated through finite element simulations and experimental validation that functionally graded thickness (FGT) tubes exhibit higher specific energy absorption than uniform-thickness (UT) tubes at the same weight, making them promising candidates for efficient energy absorption applications [24]. Zhang et al. investigated the deformation modes of thin-walled structures with variable-thickness webs under bending loads via three-point bending tests, demonstrating that concentrating material toward the web (by thinning the flanges and thickening the web) can effectively enhance bending resistance [25]. Lu et al. fabricated tailor-rolled tubes (TRTs) with axially varying thickness and, by combining axial compression experiments with finite element modeling, confirmed that optimization of the gradient transition zone and polygonal cross-sectional design are key strategies for improving the energy absorption efficiency of TRTs [26]. Similarly, Ying et al. demonstrated that FGT tubes exhibit superior crashworthiness compared to UT counterparts, simultaneously achieving higher specific energy absorption and reduced peak crushing force [27].

In recent years, artificial neural networks (ANNs), as a cornerstone of machine learning, have demonstrated significant advantages in modeling complex nonlinear systems. It is particularly suitable for dynamic coupled systems and uncertain problems that are difficult to handle by traditional methods. Relying on the improvement of computing power and data accumulation, ANNs have achieved breakthrough applications across engineering disciplines: accurately predicting turbulent velocity fields in fluid dynamics [28–33], enabling intelligent fault diagnosis in equipment maintenance [34–36], and efficiently constructing mechanical response models in materials science [37,38]. This powerful nonlinear fitting capability establishes a new paradigm for modeling complex engineering systems. Collision processes are highly nonlinear, and the crashworthiness performance of structures is significantly influenced by the coupling effects of multiple parameters. ANNs, with their powerful capability for nonlinear fitting, can directly establish the mapping relationship between design parameters and crash responses, providing an efficient and accurate new approach for predicting the performance of complex energy-absorbing structures. Compared to traditional response surface methods, this approach overcomes the limitations of linear assumptions and simplified models, demonstrating superior predictive accuracy and broad application potential in engineering fields such as train energy-absorbing devices and automotive bumpers.

Recent advances further validate this potential: Xu et al. proposed an LSTM-stacked auto-encoder architecture for multi-source response prediction, enabling both crashworthiness metric forecasting and full response curve reconstruction. Their work established a new framework integrating deep learning with optimization methodologies [39]. Yang et al. proposed a transfer learning-based inverse identification approach to solve the problem of being unable to directly measure crashworthiness indicators in railway vehicle collisions caused by the absence of sensors. This method can accurately invert structural parameters and crashworthiness indicators [40]. Guo et al. proposed a new framework for predicting the crashworthiness of square conical energy-absorbing structures (SCEAs) using machine learning. By comparing four machine learning models, they found that the gated recurrent unit (GRU) achieved the most accurate prediction of the energy absorption characteristic curve [41]. Collectively, these studies demonstrate how machine learning is driving a paradigm shift in rail vehicle safety design from experience-driven to data-driven approaches, providing transferable technical pathways for structural optimization in complex collision scenarios.

This study presents a systematic optimization framework for crashworthiness design of a variable-thickness expansion tube (VTET), integrating finite element simulation, intelligent prediction, and multi-objective decision-making. The finite element model is validated through quasi-static compression tests. An orthogonal experiment is employed to analyze the effects of key parameters—such as wall thickness and die cone angle—on energy absorption (*EA*), structural mass (*m*), and initial peak crushing force (*IPCF*). A fully connected neural network with feature importance (FI-FCN) is then developed, enabling high-accuracy prediction of nonlinear crash responses while enhancing model interpretability. The NSGA-II algorithm generates a Pareto-optimal front balancing EA, m, and IPCF. To select a single optimal solution, an entropy weight–grey relational analysis–TOPSIS (EW-GRA-TOPSIS) decision-making method is adopted, ensuring objective weighting and robust selection. Compared to conventional constant-thickness designs, the VTET achieves superior energy absorption and initial peak crush force control. Relative to traditional surrogate models (e.g., response surface methods), the proposed neural network better captures the highly nonlinear relationship between design variables and crash responses. By integrating objective weighting and comprehensive evaluation, the framework overcomes subjectivity in decision-making and enables reliable design optimization. The flowchart of the proposed optimization framework is depicted in Figure 1. In summary, the systematic optimization methodology proposed in this study not only provides an efficient and accurate technical pathway for the design of VTET, but also establishes a generalizable paradigm for multi-objective performance optimization of complex energy-absorbing structures, offering broad engineering applicability.

This work is organized as follows. Section 2 presents the axial compression experiments and finite element analysis. Section 3 employs an orthogonal test and establishes a fully connected neural network surrogate model incorporating a feature importance layer. Section 4 selects the most satisfactory configuration from the Pareto front. Conclusions are summarized in Section 5.

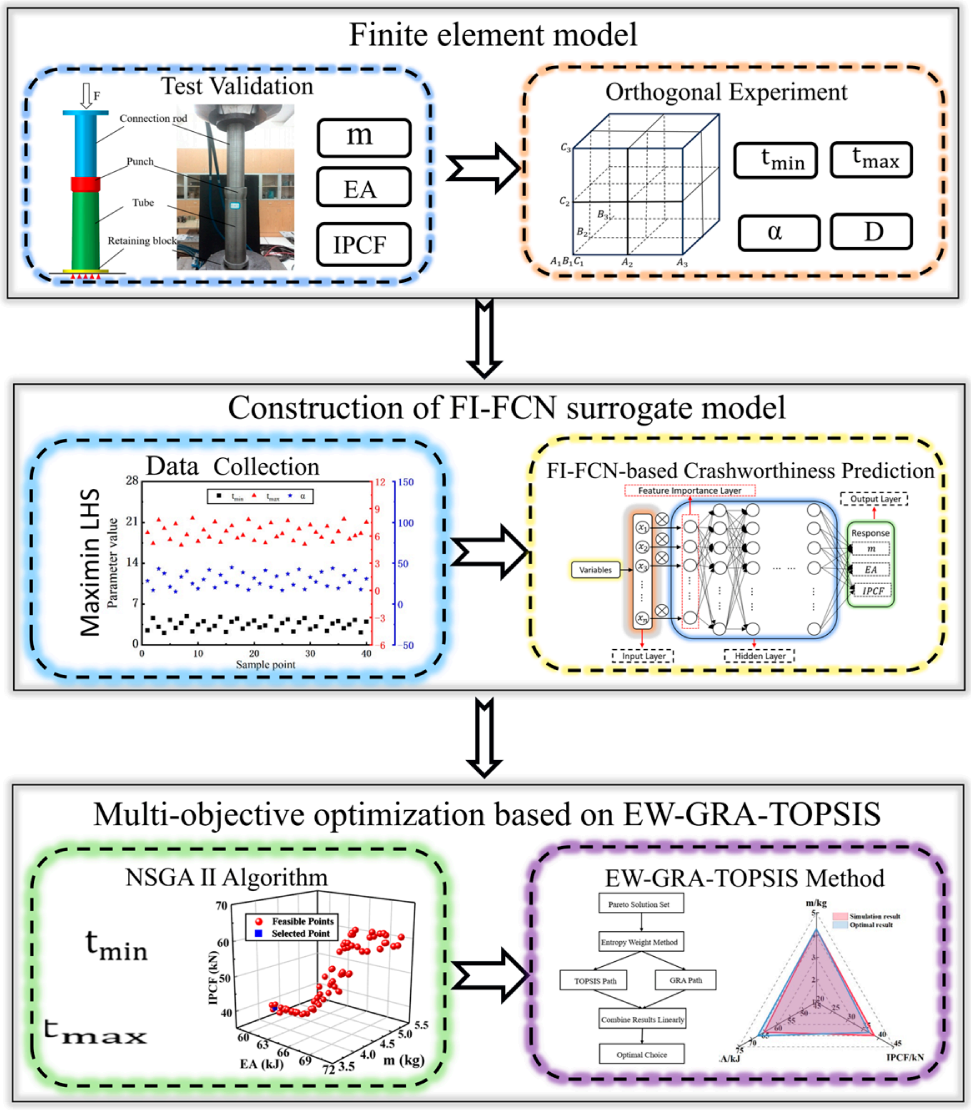


Figure 1. Flowchart of the proposed systematic optimization framework.

2. Finite Element Modeling and Test Investigation

2.1. Material Test

The tube is fabricated from 20 steel, a common engineering material characterized by its cost-effectiveness and reliable mechanical performance. The tensile specimens were prepared according to GB/T 16865-2013 [42], with dimensions detailed in Figure 2b. Quasi-static tensile tests were conducted using an MTS 647 hydraulic testing machine (MTS Systems Corporation, Eden Prairie, MN, USA) fitted with wedge grips (Figure 2a), with a constant crosshead displacement rate of 2 mm/min. The fracture morphology of the specimen after testing is presented in Figure 2c.

Figure 3a shows the engineering stress–strain curve of 20 steel. The conversion from engineering stress and strain to true stress and strain is given by Equation (1) and Equation (2), respectively.

$$\varepsilon_T = \ln(\varepsilon_E + 1) \quad (1)$$

$$\sigma_T = \sigma_E(\varepsilon_E + 1) \quad (2)$$

where σ_T is the true stress, ε_T is the true strain, σ_E is the engineering stress, and σ_E is the engineering strain.

Figure 3b displays the true stress–strain curve obtained by converting the engineering stress and strain through conventional transformation equations. A total of ten representative points were selected along the curve and approximated via piecewise linear interpolation for implementation in the finite element analysis. Based on the slope of the elastic portion, the Young's modulus is calculated as 209.3 GPa, and the 0.2% offset yield strength is identified as 308.6 MPa.

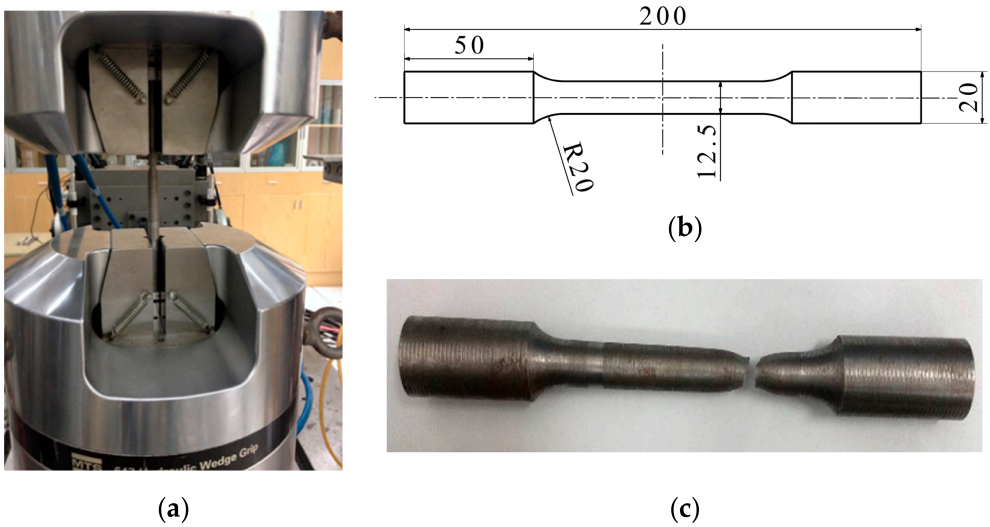


Figure 2. Quasi-static test: (**a**) testing machine, (**b**) geometry dimension of specimen (units: mm), (**c**) fracture sample.

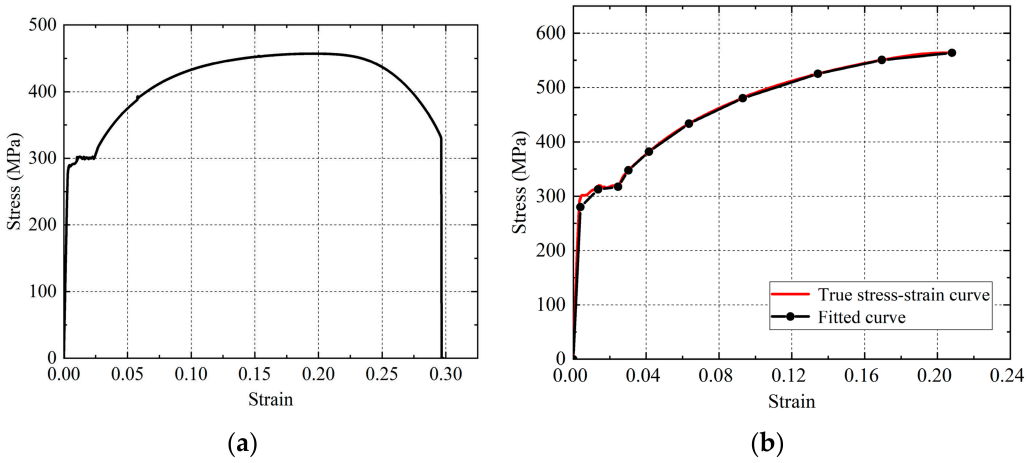


Figure 3. Constitutive behavior of 20 steel under uniaxial tension: (**a**) engineering stress–strain response; (**b**) true stress–strain relationship.

2.2. Finite Element Modeling

In this study, numerical analysis is conducted with the commercial code LS-DYNA. Figure 4 illustrates the finite element model of the VTET. The VTET model was developed using eight-node hexahedral solid elements for all components, with an element size of 1.0 mm × 1.0 mm × 1.0 mm. A single-point integration scheme with stiffness-based hourglass control was employed to ensure numerical stability while maintaining computational efficiency. The Belytschko-Tsay explicit dynamic algorithm was employed to solve the dynamic equations, offering high computational efficiency and robustness for simulating large-deformation impact events. The 20 steel material behavior of the tube was modeled using the modified piecewise linear plasticity model (*MAT_MODIFIED_PIECEWISE_LINEAR_PLASTICITY, MAT123) in LS-DYNA. Material

density ρ = 7800 kg/m3, the Young's modulus E = 209.3 GPa, Poisson's ratio v = 0.3, and initial yield stress σ_y = 308.6 MPa. A fully fixed boundary condition was applied to the bottom end of the expansion tube to simulate clamped support. Contact interactions between the punch and the tube were modeled using the automatic surface-to-surface contact algorithm (*CONTACT_AUTOMATIC_SURFACE_TO_SURFACE) with a penalty-based formulation. To accurately represent the frictional behavior, the coefficient of friction was determined through an inverse calibration approach by matching the simulated force–displacement curve to experimental data. A friction coefficient of 0.112 was found to provide the best agreement between simulation and test.

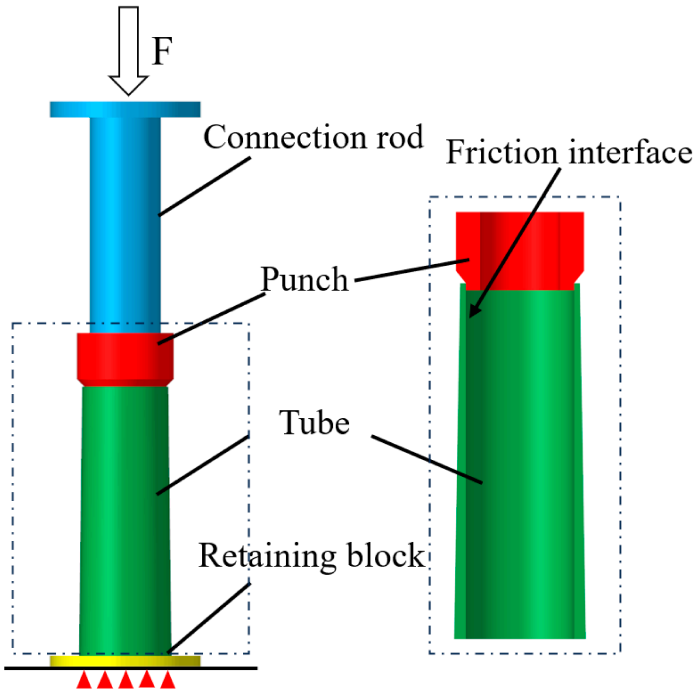


Figure 4. Finite element model.

2.3. Quasi-Static Axial Compression Test

To establish the reliability of the numerical model, this study first selected the uniform thickness expansion tube (UTET) as a baseline model for experimental validation. By systematically correlating the simulation results with the experimentally obtained load–displacement curves and deformation modes of the UTET, key modeling parameters were comprehensively calibrated. Given that the variable thickness expansion tube (VTET) shares the same base material, manufacturing process, and underlying mechanical response mechanisms with the UTET, the simulation methodology rigorously validated through the UTET can be reasonably extended to predict the mechanical behavior of the VTET. Consequently, although physical prototypes of the VTET were not fabricated in this phase, the numerical model is considered to possess sufficient fidelity to support subsequent parametric studies and design optimization.

The experimental setup is illustrated in Figure 5. Quasi-static loading tests were conducted using a hydraulic testing machine (MTS322) with a maximum load capacity of 500 kN. An air vent hole was designed on the retaining block to release air generated during the compression process. Prior to testing, the positions of the connecting rod, expansion tube, and punch were adjusted to ensure alignment of their axes with that of the testing machine. S1M32 hydraulic oil was applied to lubricate the contact interface between the expansion tube and the punch, thereby reducing friction. A preload of 10 N was applied to each specimen to ensure symmetrical shrinkage during compression. Subsequently,

the crosshead of the testing machine pressed the punch into the tube at a constant speed of 5 mm/min. The compressive load was continuously applied until the stroke reached 150 mm. Four punches with different cone angles (15°, 25°, 35°, and 45°) were tested, and their geometries are shown in Figure 6.

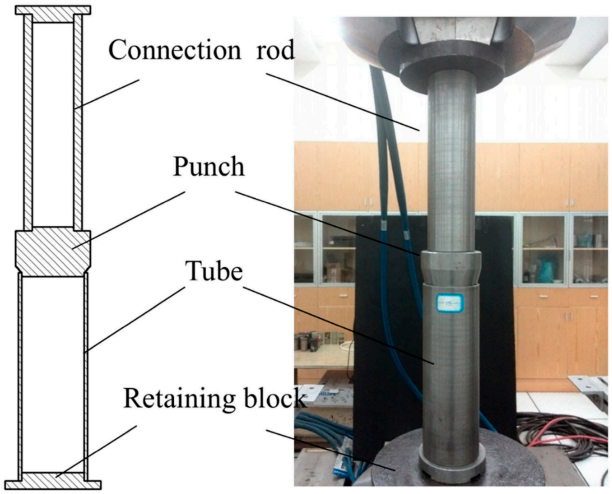


Figure 5. Sketch of the experimental setup.

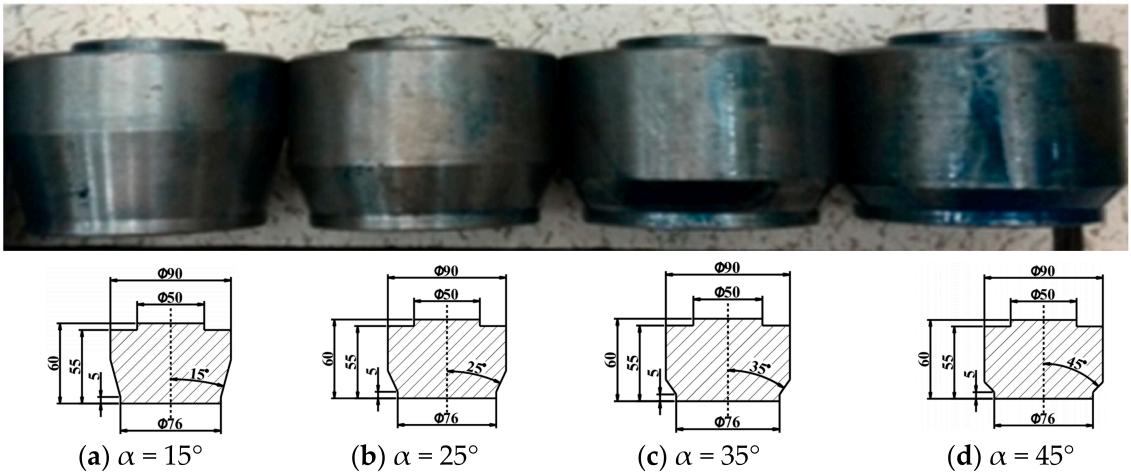


Figure 6. Four types of punches with different cone angles: (**a**) α = 15°, (**b**) α = 25°, (**c**) α = 35°, (**d**) α = 45° (length unit: mm).

Figure 7 shows the relationship between compressive force and displacement from four sets of quasi-static tests. All tests under different punch cone angles exhibit similar load–displacement trends, and the compressive force increases with increasing cone angle. The loading process can be divided into the following three stages: Upon initial contact between the tube and the punch, a small indentation load appears due to localized deformation. As the punch moves downward, the contact area between the punch and the tube increases progressively, while the tube undergoes continuous expansion deformation under the action of the punch, leading to a sharp rise in the load. Once the tube fully conforms to the punch, the system reaches force equilibrium, resulting in a stable steady-state load.

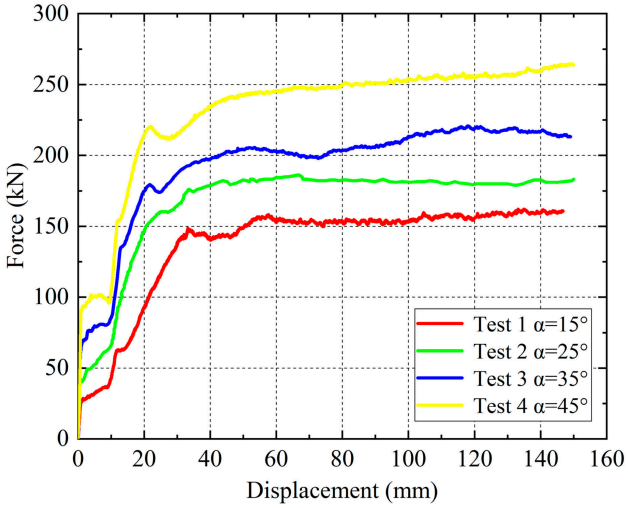


Figure 7. The compressive force–displacement curves of the four tests.

The force–displacement responses and deformation modes from both experiments and simulations for the UTET are presented in Figure 8. A close agreement between the numerical predictions and experimental results can be observed, particularly in terms of load trends and overall deformation patterns. This good correlation validates the accuracy of the developed finite element model, providing confidence in its use for further investigation into the energy absorption characteristics of the VTET and subsequent structural optimization.

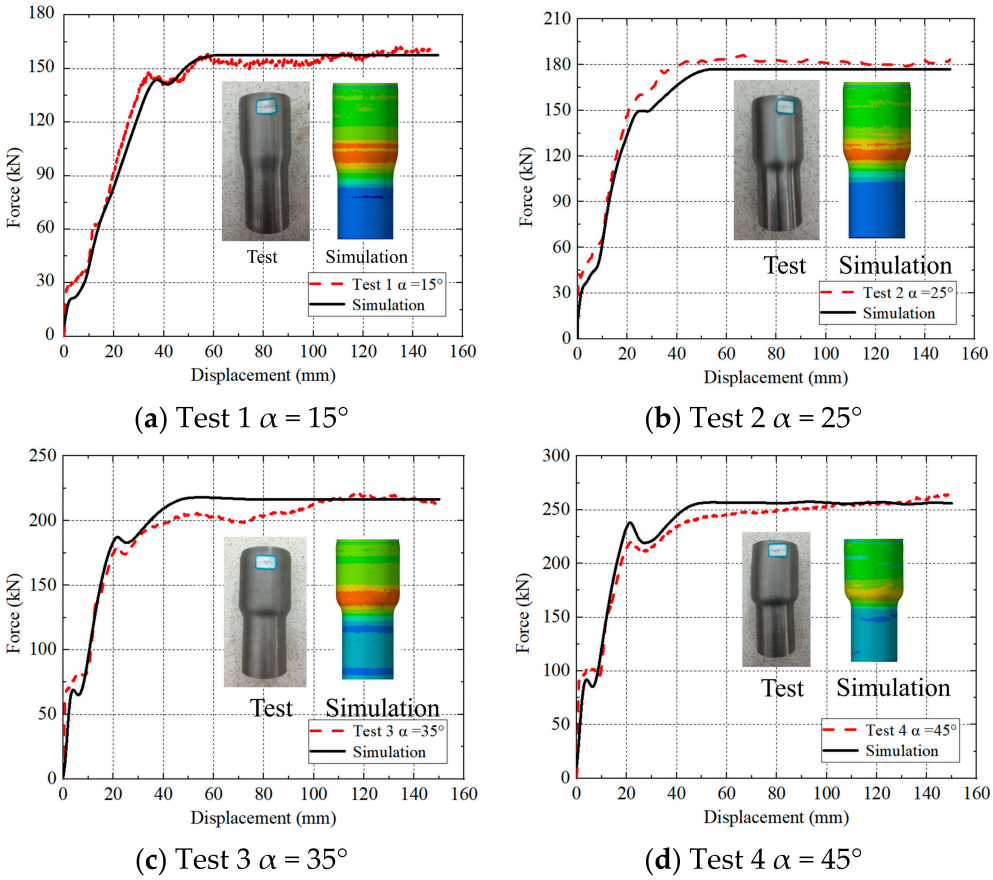


Figure 8. Comparison of force–displacement curves from experiments and simulations for the four test cases.

3. Orthogonal Test Analysis and Construction of the Fully Connected Network with Feature Importance (FI-FCN)

3.1. Orthogonal Test Analysis

Orthogonal test results can be evaluated using variance analysis [43]. This statistical approach enables the differentiation between variations in experimental outcomes attributable to changes in factor levels and those arising from random errors, thereby enhancing the reliability and accuracy of the analysis. In this study, an orthogonal experimental design based on the $L_{16}(4^3)$ orthogonal array was employed to investigate the effects of four key parameters and their interactions on the response variables—initial peak crushing force (*IPCF*), energy absorption (*EA*), and structural mass (*m*). The selected factor levels for the orthogonal experiments are summarized in Table 1. As shown in Figure 9, $t_{\min}$ denotes the minimum wall thickness, $t_{\max}$ denotes the maximum wall thickness, and *D* denotes the inner diameter of the circular tube. The design parameters are graphically described in Figure 9.

Table 1. Orthogonal test factors and levels.

Levels	Experimental Factor			
	$t_{\min}$ (mm)	$t_{\max}$ (mm)	α (°)	D (mm)
1	2	5	15	76
2	3	6	25	78
3	4	7	35	80
4	5	8	45	82

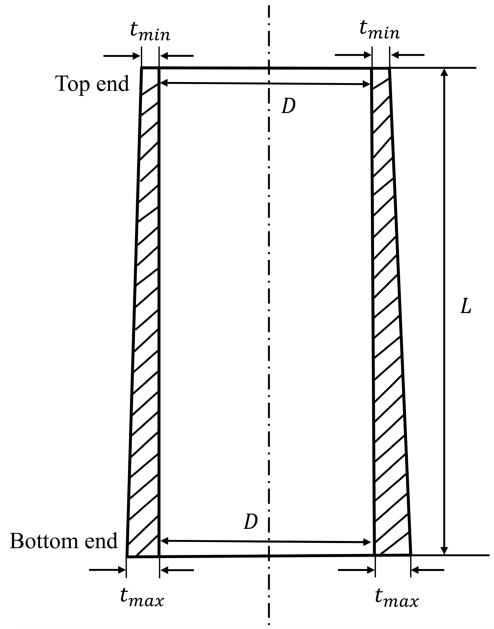


Figure 9. Cross-sectional dimensions of the thickness-graded tube.

To evaluate the performance under each experimental condition, numerical simulations were conducted according to the 16 trial runs specified in the orthogonal array. For each run, the values of m, EA, and IPCF were obtained through simulation, with the complete set of results presented in Table 2. The simulation results were then analyzed using analysis of variance (ANOVA) to quantify the contribution of each factor and to determine its statistical significance. In ANOVA, the sum of squares (SS) and mean square (MS) for each factor were calculated, and the F-ratio was used to test the significance level, with a

confidence threshold of β = 0.05. This approach enables the identification of dominant factors influencing the responses and provides a scientific basis for parameter optimization.

Table 2. Simulation results of the 16-run orthogonal experimental design.

No.	t_{min} (mm)	t_{max} (mm)	α (°)	*D* (mm)	*IPCF* (kN)	*EA* (kJ)	*m* (kg)
1	2.00	5.00	15.00	76.00	14.59	14.01	2.86
2	2.00	6.00	25.00	78.00	19.84	27.24	3.24
3	2.00	7.00	35.00	80.00	27.37	42.11	3.57
4	2.00	8.00	45.00	82.00	33.46	59.87	3.64
5	3.00	5.00	25.00	80.00	31.88	25.60	3.28
6	3.00	6.00	15.00	82.00	17.74	17.60	3.43
7	3.00	7.00	45.00	76.00	59.48	75.52	3.72
8	3.00	8.00	35.00	78.00	45.62	58.01	3.98
9	4.00	5.00	35.00	82.00	66.76	40.10	3.60
10	4.00	6.00	45.00	76.00	85.41	69.56	3.72
11	4.00	7.00	15.00	78.00	25.23	26.98	3.80
12	4.00	8.00	25.00	80.00	45.42	42.17	4.21
13	5.00	5.00	45.00	78.00	127.62	69.34	3.77
14	5.00	6.00	35.00	76.00	87.91	58.87	3.91
15	5.00	7.00	25.00	82.00	56.82	38.70	4.27
16	5.00	8.00	15.00	80.00	33.87	30.57	4.33

For the response variable m, the *p*-values of the factors t_{min}, t_{max}, α, and *D* are 0.002, 0.004, 0.134, and 0.540, respectively. Applying a significance threshold of β = 0.05, t_{min} and t_{max} are clearly identified as statistically significant predictors of m. Although α does not reach conventional significance ($p = 0.134 > 0.05$), it exhibits a marginal association and is retained due to its physical relevance in the underlying mechanism, which is theoretically linked to m. In contrast, *D* ($p = 0.540$) shows no meaningful association and is excluded from further analysis. To reflect the relative strength of statistical evidence among the retained factors, initial feature weights were assigned based on $-\log_{10}(p)$ values, which quantify the degree of deviation from the null hypothesis. After normalization, the resulting initial weights for t_{min}, t_{max}, and α are 0.452, 0.402, and 0.146, respectively.

Similarly, for the response variable *IPCF*, the *p*-values of the factors t_{min}, t_{max}, α, and *D* are 0.022, 0.023, 0.027, and 0.618, respectively. The factors t_{min}, t_{max}, and α are identified as significant factors influencing *IPCF*. In contrast, *D* has no significant effect and may be neglected in further analysis. For the response variable EA, the *p*-values of the factors t_{min}, t_{max}, α, and *D* are 0.012, 0.017, 0.001, and 0.039, respectively. All four factors are statistically significant and therefore identified as predictors of *EA*. However, given that *D* is not significant in the analyses of m and *IPCF*, and to ensure model consistency and interpretability across responses, *D* was excluded from further analysis. Therefore, only t_{min}, t_{max}, and α were retained as input features in subsequent modeling.

3.2. Construction of FI-FCN Surrogate Model

Maximin Latin Hypercube Sampling (Maximin LHS) was selected for experimental design due to its superior spatial coverage, which maximizes the minimum inter-point distance to ensure uniform sample distribution across the design space. Parameters were set as t_{min}: 2.00 mm~5.00 mm, t_{max}: 5.00 mm~8.00 mm, and α: 15°~45°. The generated samples (Table 3) were used to construct surrogate models.

Table 3. Maximin LHS sampling results.

No.	t_{min} (mm)	t_{max} (mm)	α (°)	*IPCF* (kN)	*EA* (kJ)	*m* (kg)
1	2.47	6.37	28.32	25.85	36.42	3.91
2	4.62	5.18	16.98	28.42	28.24	3.92
3	3.09	7.76	43.14	62.15	75.13	4.53
4	2.05	6.83	37.65	36.04	48.01	4.01
5	4.23	5.61	21.03	34.03	33.22	4
6	2.88	7.34	15.1	17.56	27.22	4.22
7	3.76	5.02	33.47	54.70	41.67	3.76
8	4.94	6.15	40.28	94.25	70.97	4.4
9	2.31	7.97	24.89	40.79	39.43	4.38
10	3.45	5.42	18.76	25.80	26.68	3.76
11	4.01	6.67	30.15	56.53	48.94	4.34
12	2.63	5.89	42.05	42.76	51.54	3.83
13	3.27	7.55	19.92	26.34	35.02	4.42
14	4.78	5.31	35.67	74.89	53.99	4.09
15	2.19	6.54	26.44	38.61	33.68	3.9
16	3.92	7.13	44.81	86.21	80.15	4.51
17	4.46	5.76	22.39	42.53	35.93	4.11
18	2.75	6.08	38.73	43.01	49.17	3.91
19	3.58	7.82	17.25	24.67	33.63	4.55
20	4.14	5.5	31.88	59.14	44.90	4
21	2.96	6.91	25.07	29.72	37.90	4.18
22	3.33	5.24	41.2	60.89	50.04	3.77
23	4.81	7.45	20.56	43.74	42.22	4.72
24	2.52	5.93	34.11	33.02	40.59	3.8
25	3.7	6.26	16.78	19.45	28.42	4.06
26	4.35	7.68	36.94	79.09	71.44	4.76
27	2.24	5.47	23.5	39.09	26.51	3.56
28	3.84	6.79	42.63	77.55	71.38	4.38
29	4.59	5.11	18.04	34.27	28.97	3.89
30	2.69	7.22	32.77	32.89	48.46	4.25
31	3.16	6.41	27.13	34.33	38.68	4.07
32	4.72	5.85	39.45	85.82	64.64	4.26
33	2.38	7.07	21.88	20.28	31.80	4.08
34	3.64	5.33	43.76	72.14	57.89	3.87
35	4.08	6.5	19.22	33.20	33.45	4.24
36	2.82	7.88	35.01	41.11	57.55	4.5
37	3.49	5.67	26.34	37.08	35.97	3.88
38	4.28	6.04	41.59	89.44	66.85	4.22
39	2.13	6.3	17.67	18.32	23.89	3.75
⋮	⋮	⋮	⋮	⋮	⋮	⋮
100	3.98	7.51	30.88	64.83	61.25	4.63

Based on these experimental samples, surrogate modeling has become an effective approach for achieving efficient and accurate optimization in complex engineering problems. Commonly used surrogate models include response surface methodology, Kriging, radial basis functions, and polynomial response surfaces, all of which have demonstrated effectiveness in crashworthiness design [44]. However, as the nonlinearity and complexity of engineering problems increase, traditional surrogate models often suffer from insufficient fitting accuracy or poor generalization when handling high-dimensional, strongly nonlinear relationships. To address this limitation, this paper introduces a FI-FCN -based surrogate model that fully leverages the high-quality data provided by Maximin LHS to better

capture the complex nonlinear mappings between design variables and response metrics (e.g., *IPCF*, *EA*, *m*), thereby improving prediction accuracy and model robustness.

The architecture of the proposed fully connected neural network is illustrated in Figure 10. As shown, the network consists of four main components: an input layer, a feature importance layer, multiple hidden layers, and an output layer. The first layer serves as the input layer, where the design variables of the VTET structure are fed into the network as features. The second layer is the specially designed feature importance layer, which assigns weighting coefficients to each input feature based on the results of orthogonal array experiments, quantifying the influence of each design variable on the target responses. This mechanism not only adaptively enhances critical design variables but also suppresses interference from redundant ones, thereby improving model convergence speed and interpretability. After weighted scaling in the feature importance layer, the data are passed to a series of fully connected hidden layers. Two hidden layers are employed in this study, containing 32 and 64 neurons respectively. By incorporating nonlinear activation functions such as ReLU, the network can progressively extract higher-order features and learn the underlying nonlinear relationships between inputs and outputs. Finally, after mapping through the output layer, the model predicts key performance indicators—namely, the initial peak crushing force (*IPCF*), energy absorption (*EA*), and structural mass (*m*). This establishes three surrogate models for subsequent multi-objective optimization.

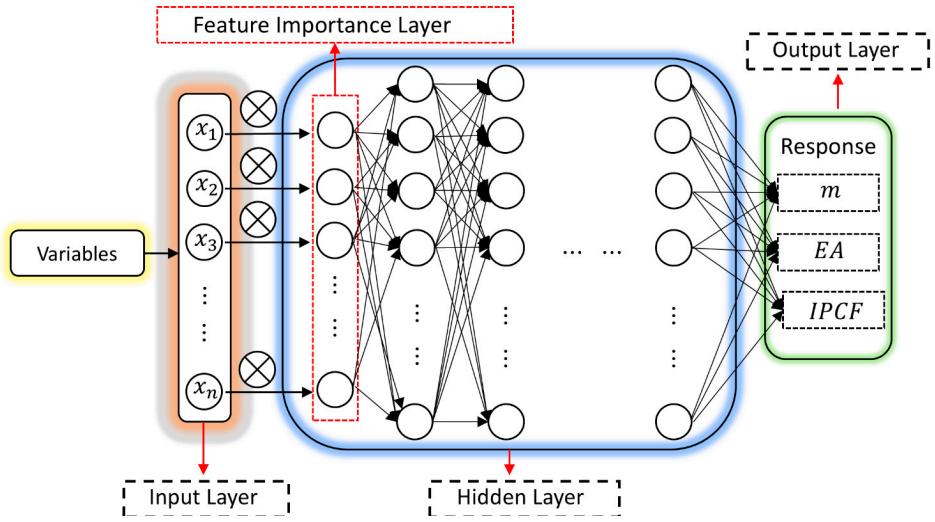


Figure 10. Schematic of FCNN model.

To ensure the accuracy and generalization capability of the developed neural network surrogate model, a 5-fold cross-validation procedure is conducted to comprehensively evaluate its predictive performance. Specifically, the entire dataset is randomly partitioned into five equally sized, non-overlapping subsets. In each fold, one subset is used as the validation set while the remaining four are utilized for training. This process is repeated five times so that each subset serves once as the validation set. The final evaluation metrics—namely the coefficient of determination (R^2), root mean squared error (RMSE), mean absolute error (MAE), and mean absolute percentage error (MAPE)—are reported as the average values across all five folds. This approach effectively mitigates bias caused by arbitrary data splitting and provides a robust assessment of the model's stability and generalization on unseen samples.

The performance metrics are defined as follows:

$$R^2 = 1 - \frac{\sum_{i=1}^{n} (y_i - \hat{y}_i)^2}{\sum_{i=1}^{n} (y_i - \overline{y}_i)^2} \tag{3}$$

$$RMSE = \sqrt{\frac{1}{n}\sum_{i=1}^{n}(y_i - \hat{y}_i)^2} \tag{4}$$

$$MAE = \frac{1}{n}\sum_{i=1}^{n}|y_i - \hat{y}_i| \tag{5}$$

$$MAPE = \frac{100\%}{n}\sum_{i=1}^{n}\left|\frac{y_i - \hat{y}_i}{y_i}\right| \tag{6}$$

where y_i denotes the ith true value, $\hat{y}_i$ denotes the i-th predicted value from the surrogate model, $\overline{y}_i$ represents the mean of true values, and n is the total number of samples.

The proposed FI-FCN was evaluated using this method, and the results are summarized in Table 4. As shown, the model achieves R^2 values all exceeding 0.95, alongside consistently low RMSE, MAE, and MAPE across all response variables. These results confirm the effectiveness and robustness of the FI-FCN model in constructing surrogate models for VTET crashworthiness optimization.

Table 4. Performance evaluation results of the FI-FCN model.

Model	R^2	RMSE	MAE	MAPE
EA	0.985	1.769 kJ	1.230 kJ	2.417%
IPCF	0.953	4.380 kN	3.375 kN	9.738%
m	0.995	0.018 kg	0.013 kg	0.326%

4. Multi-Objective Optimization Based on EW-GRA-TOPSIS

4.1. EW-GRA-TOPSIS Method

To overcome the limitations of traditional multi-attribute decision-making methods, this study proposes a hybrid evaluation framework integrating the Entropy Weight Method (EWM), Technique for Order Preference by Similarity to Ideal Solution (TOPSIS), and Grey Relational Analysis (GRA). The complete workflow is illustrated in Figure 11. The model follows a three-stage procedure: objective weighting, dual-path assessment, and coordinated integration, enabling a scientific and comprehensive evaluation of design alternatives.

First, the EWM is employed to determine objective weights for each indicator, thereby avoiding systematic biases introduced by expert-based subjective weighting. Specifically, the dispersion of indicator values across different schemes is used to reflect their information content, based on which the weight vector W = (w_1, w_2, w_3) is derived, ensuring that the weighting process is fully data-driven.

Second, on the basis of a unified weighted and normalized decision matrix, two complementary evaluation pathways are executed in parallel:

(1) TOPSIS path: Measures the Euclidean distance between each alternative and the ideal/anti-ideal solutions, emphasizing "geometric proximity" in the numerical space.

(2) GRA path: Computes grey relational degrees by analyzing the similarity in curve shape between sequences, capturing the "trend consistency" between alternatives and ideal solutions. This approach is particularly effective in scenarios involving small sample sizes or strong nonlinearity.

Finally, to integrate the complementary advantages of distance proximity and trend similarity, a composite evaluation model is developed. After normalizing the TOPSIS relative closeness (d_i) and the GRA relative relational degree (γ_i), a linear weighted fusion approach is employed to derive the overall comprehensive evaluation score O_{i}^{*}:

$$O_{\mathrm{i}}^{*} = \frac{\alpha D_{\mathrm{i}}^{-} + \beta E_{i}^{+}}{\alpha D_{\mathrm{i}}^{-} + \beta E_{i}^{+} + \alpha D_{\mathrm{i}}^{+} + \beta E_{i}^{-}} \tag{7}$$

where $D_{i}^{\pm}$ and $E_{\mathrm{i}}^{\pm}$ denote the normalized values from TOPSIS and GRA, respectively, and α and β are weighting coefficients (set as $\alpha = \beta = 0.5$ in this study), reflecting the equal importance assigned to both evaluation dimensions.

By integrating the strengths of entropy weighting, TOPSIS, and GRA, the proposed hybrid model achieves enhanced robustness and a more holistic representation of decision outcomes, demonstrating strong applicability to complex engineering problems with uncertain and conflicting criteria, including vehicle crashworthiness design.

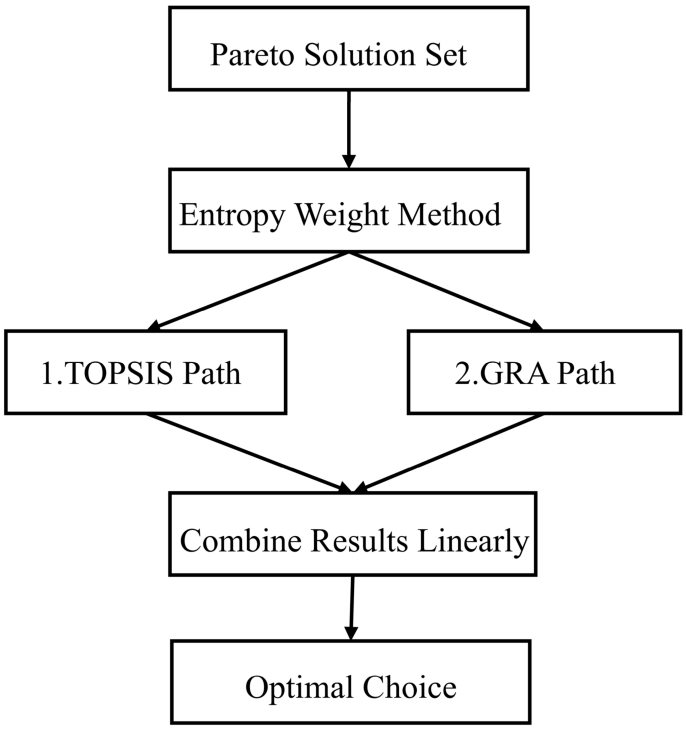


Figure 11. Schematic of EW-GRA-TOPSIS method.

4.2. Multi-Objective Optimization Model

In order to achieve optimal crashworthiness performance metrics, it is necessary to optimize the structural parameters of the VTET. If we suppose $\mathrm{f}_1(t_{\min}, t_{\max}, \alpha) = IPCF$, $\mathrm{f}_2(t_{\min}, t_{\max}, \alpha) = EA$, and $\mathrm{f}_3(t_{\min}, t_{\max}, \alpha) = m$, then the objective function satisfies the following constraints.

$$\begin{cases} \text{Min } \mathrm{f}_1(t_{\min}, t_{\max}, \alpha) \\ \text{Max } \mathrm{f}_2(t_{\min}, t_{\max}, \alpha) \\ \text{Min } \mathrm{f}_3(t_{\min}, t_{\max}, \alpha) \end{cases} \tag{8}$$

$$\text{Subject to } \begin{cases} 2.0 \text{ mm} < t_{min} < 5.0 \text{ mm} \\ 5.0 \text{ mm} < t_{max} < 8.0 \text{ mm} \\ 15^{\circ} < \alpha < 45^{\circ} \end{cases} \tag{9}$$

To obtain the optimal design of the VTET, a non-dominated sorting genetic algorithm II (NSGA-II) is employed, with its parameters detailed in Table 5. The Pareto front of the VTET is shown in Figure 12. It can be observed that the Pareto front exhibits a well-distributed and continuous curve, indicating a good trade-off between the conflicting objectives—*m*, *IPCF*, and *EA*. This diversity and spread of solutions provide designers with a wide range of feasible options, each representing different performance compromises. However, since all solutions on the Pareto front are non-dominated and thus incomparable in a multi-objective context, it becomes challenging to select a single best solution for practical engineering applications. Therefore, an integrated decision-making method combining EW, GRA, and TOPSIS is subsequently employed to rank the Pareto-optimal solutions and identify the most balanced and comprehensive optimal design based on objective weighting and relative closeness to the ideal solution. This approach ensures a more rational and systematic selection process, taking into account both the importance of each objective and the overall performance of candidate designs.

Table 5. The setting of the multi-objective genetic algorithm NSGA-II.

Parameters	Values
Population size μ	60
Offspring size λ	50
Maximum number of iterations	300
Mutation rate	0.1
Crossover rate	0.8

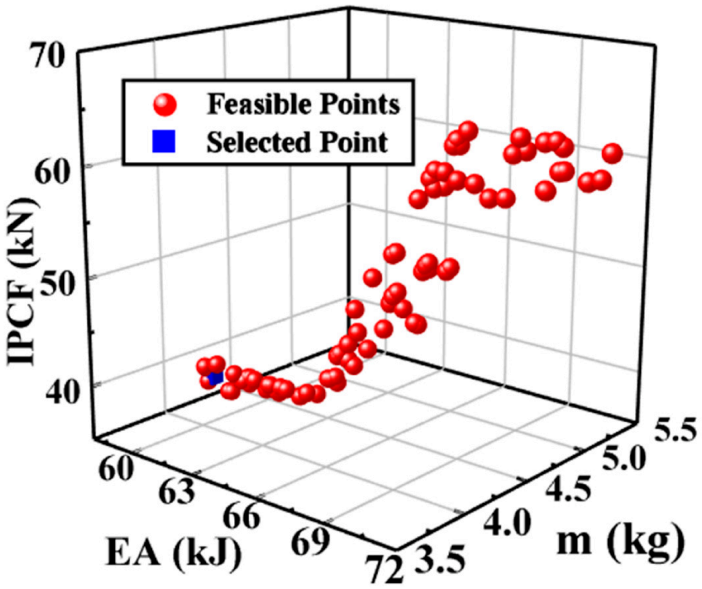


Figure 12. Pareto solution set.

4.3. Optimization Result

This paper introduces a three-stage collaborative evaluation framework integrating the EWM, TOPSIS, and GRA. Without requiring subjective weight assignment, this method comprehensively evaluates the geometric proximity of candidate solutions to the ideal solution in numerical space and the consistency of indicator evolution trends, ultimately identifying a compromise solution on the Pareto front that combines performance superiority with structural coherence.

Specifically, the objective weights of each objective function are first calculated using EWM based on the variation degree of their values within the Pareto solution set. Results indicate that *IPCF* has the highest weight (w = 0.443), demonstrating significant vari-

ation across candidate solutions and strong discriminative capability, making it a key factor influencing the final decision. Conversely, EA has a relatively lower weight of 0.251, reflecting its concentrated value distribution and limited information discrimination capacity. Subsequently, TOPSIS is employed to calculate the closeness coefficient of each solution to the positive and negative ideal solutions, while GRA assesses the relational grade between each solution and the ideal reference sequence. To further enhance the robustness and multidimensional representation of the evaluation, a nonlinear fusion approach integrates these two scores to derive a comprehensive evaluation value for each candidate solution.

In this study, solution No. 145 (t_{min} = 2.08 mm, t_{max} = 7.62 mm, α = 44.90°) achieved the highest comprehensive score and was selected as the final recommended solution. This solution is highlighted as a blue dot on the Pareto front in Figure 12. To verify the accuracy of the optimization results, the optimal parameter configuration was evaluated through finite element simulation, with comparative results detailed in Table 6. The *EA* values for the optimization prediction and finite element simulation were 67.68 kJ and 65.21 kJ, respectively, with relative errors for m and *IPCF* being 0.23% and 4.37%, all below the engineering-acceptable threshold of 5%. This confirms the reliability of the optimization results. Figure 13 presents a radar chart comparison of the optimization and simulation results, showing consistency across all performance indicators and further validating the effectiveness of the proposed method.

Table 6. Comparison between the optimization results and simulation results.

	m (kg)	*EA* (kJ)	*IPCF* (kN)
Optimal result	4.27	65.21	38.68
Simulation result	4.28	67.68	37.06
Relative error	0.23%	3.65%	4.37%

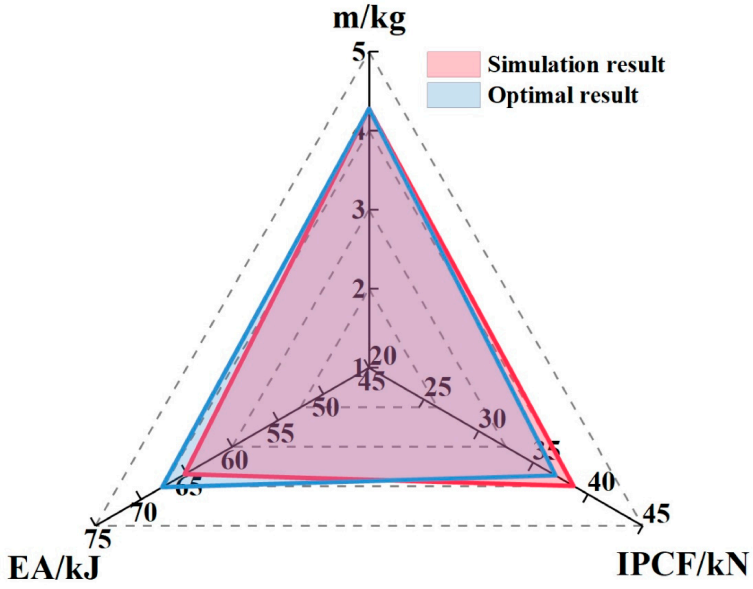


Figure 13. Radar chart comparing the EW-GRA-TOPSIS selected optimal design with simulation results.

5. Conclusions

This study investigates the crashworthiness of a VTET structure, with the finite element model validated through quasi-static compression tests on a UTET prototype. An orthogonal array test was conducted to quantify the relative influence of design variables

(t_{min}, t_{max}, α, D) on key crashworthiness indicators: *EA*, *IPCF*, and *m*. Results show that t_{min}, t_{max}, α are statistically significant factors influencing *EA* and *IPCF*, with *p*-values below the 0.05 threshold. Although α shows marginal significance in the m (p = 0.134), it is retained in the analysis owing to its physical relevance in geometric configuration. In contrast, *D* shows no consistent significance across the response variables, being non-significant for both m and *IPCF*. Therefore, it is excluded from further modeling to improve interpretability and model consistency.

A fully connected network with feature importance (FI-FCN) was developed as a surrogate model for *EA*, *m*, and *IPCF*. Five-fold cross-validation demonstrates robust predictive performance, yielding coefficients of determination (R^2) exceeding 0.95 for all targets (*EA*: 0.985, m: 0.995, *IPCF*: 0.953).

Using the NSGA-II algorithm, the Pareto front was generated, from which the optimal design (t_{min} = 2.08 mm, t_{max} = 7.62 mm, α = 44.90°) was selected via the integrated EW-GRA-TOPSIS decision-making approach. Finite element simulations confirm the reliability of this solution, with relative errors between predicted and simulated values below 5% (*EA*: 3.65%, *m*: 0.23%, *IPCF*: 4.37%).

The proposed integrated workflow—combining orthogonal testing, feature importance analysis, surrogate modeling, multi-objective optimization, and hybrid decision-making—demonstrates strong applicability and effectiveness in crashworthy structural design, offering a systematic framework for engineering practice.

Author Contributions: Conceptualization, D.Y. and W.G.; methodology, D.Y.; software, J.L.; validation, Z.L., H.D. and J.L.; formal analysis, J.L.; investigation, D.Y.; resources, D.Y.; data curation, D.Y.; writing—original draft preparation, D.Y.; writing—review and editing, W.G.; visualization, J.L.; supervision, Z.L.; project administration, Z.L.; funding acquisition, W.G. All authors have read and agreed to the published version of the manuscript.

Funding: This work was supported by the Natural Science Foundation of Hunan Province under Grant No. 2024JJ6519.

Data Availability Statement: The data presented in this study are available on request from the corresponding author.

Acknowledgments: The author thanks the reviewers and editors for their criticism and guidance.

Conflicts of Interest: Authors Dezhuang Yu, Haitao Dong, Zhanyu Liu were employed by the company CRRC Dalian Locomotive and Rolling Stock Co., Ltd. The remaining authors declare that the research was conducted in the absence of any commercial or financial relationships that could be construed as a potential conflict of interest.

Abbreviations

The following abbreviations are used in this manuscript:

IPCF	Initial Peak Crushing Force
EA	Energy Absorption
m	Structural Mass
VTET	Variable Thickness Expansion Tube
FI-FCN	Fully Connected Network with Feature Importance
EWM	Entropy Weight Method
TOPSIS	Technique for Order Preference by Similarity to Ideal Solution
GRA	Grey Relational Analysis
EW-GRA-TOPSIS	Entropy Weight–Grey Relational Analysis–TOPSIS
RMSE	Root Mean Squared Error
MAE	Mean Absolute Error
MAPE	Mean Absolute Percentage Error

References

1. Forsberg, R.; Björnstig, U. One hundred years of railway disasters and recent trends. *Prehosp. Disaster Med.* **2011**, *26*, 367–373. [CrossRef] [PubMed]
2. Gao, G.; Wang, S. Crashworthiness of passenger rail vehicles: A review. *Int. J. Crashworthiness* **2019**, *24*, 664–676. [CrossRef]
3. Li, H.; Qiu, J.; Li, T.; Xie, G.; Wang, D.; Wang, W. Multiple-criteria evaluation of thin-walled energy-absorbing structures of train under fuzzy environment: Modeling and algorithm. *IEEE Access* **2021**, *9*, 156782–156794. [CrossRef]
4. State Railway Administration of the People's Republic of China. *Crashworthiness Requirements and Verification Specification for Car Body of EMU/DMU, Railway Industry Standard of the People's Republic of China*; National Railway Administration: Beijing, China, 2018.
5. Federal Railroad Administration. *49 Part 238 Subpart E Specific Requirements for Tier 2 Passenger Equipment*; The National Technical Information Service: Washington, DC, USA, 2010.
6. Technical Committee CEN/TC 256 Railway Applications. *BS EN 15227-2020*; Railway Applications: Crashworthiness Requirements for Railway Vehicle Bodies. British Standard Institution: London, UK, 2020.
7. Almeida, B.; Alves, M.; Rosa, P. Expansion and reduction of thin-walled tubes using a die: Experimental and theoretical investigation. *Int. J. Mach. Tools Manuf.* **2006**, *46*, 1643–1652. [CrossRef]
8. Li, J.; Gao, G.; Guan, W.; Wang, S.; Yu, Y. Experimental and numerical investigations on the energy absorption of shrink circular tube under quasi-static loading. *Int. J. Mech. Sci.* **2018**, *136*, 284–294. [CrossRef]
9. Choi, W.M.; Kim, J.S.; Jung, H.S.; Kwon, T.S. Effect of punch angle on energy absorbing characteristics of tube-type crash elements. *Int. J. Automot. Technol.* **2011**, *12*, 383–389. [CrossRef]
10. Venkateswarlu, G. A study on effect of process parameters on the expansion of thin walled aluminium 7075 tubes. *Int. J. Adv. Sci. Technol.* **2011**, *37*, 1–10.
11. Yan, J.; Yao, S.; Xu, P.; Peng, Y.; Shao, H.; Zhao, S. Theoretical prediction and numerical studies of expanding circular tubes as energy absorbers. *Int. J. Mech. Sci.* **2016**, *105*, 206–214. [CrossRef]
12. Shakeri, M.; Salehghaffari, S.; Mirzaeifar, R. Expansion of circular tubes by rigid tubes as impact energy absorbers: Experimental and theoretical investigation. *Int. J. Crashworthiness* **2007**, *12*, 493–501. [CrossRef]
13. Luanin, V.; Tanaskovi, J.; Milkovi, D.; Golubović, S. Experimental Research of the Tube Absorbers of Kinetic Energy During Collision. *FME Trans.* **2007**, *35*, 201–204.
14. Choi, M.; Kwon, S.; Jung, S.; Kim, J. Influence of impact velocity on energy absorption characteristics and friction coefficient of expansion tube. *Int. J. Crashworthiness* **2012**, *17*, 621–629. [CrossRef]
15. Yang, J.; Luo, M.; Hua, Y.; Lu, G. Energy absorption of expansion tubes using a conical–cylindrical die: Experiments and numerical simulation. *Int. J. Mech. Sci.* **2010**, *52*, 716–725. [CrossRef]
16. An, X.; Gao, Y.; Fang, J.; Sun, G.; Li, Q. Crashworthiness design for foam-filled thin-walled structures with functionally lateral graded thickness sheets. *Thin-Walled Struct.* **2015**, *91*, 63–71. [CrossRef]
17. Fang, J.; Gao, Y.; Sun, G.; Zheng, G.; Li, Q. Dynamic crashing behavior of new extricable multi-cell tubes with a functionally graded thickness. *Int. J. Mech. Sci.* **2015**, *103*, 105–116. [CrossRef]
18. Ding, X.; Tong, Z.; Liu, Y.; Liu, S. Dynamic axial crush analysis and design optimization of a square multi-cell thin-walled tube with lateral variable thickness. *Int. J. Mech. Sci.* **2018**, *135*, 13–26. [CrossRef]
19. Rogala, M.; Gajewski, J.; Ferdynus, M. The Effect of Geometrical Non-Linearity on the Crashworthiness of Thin-Walled Conical Energy-Absorbers. *Materials* **2020**, *13*, 4857. [CrossRef] [PubMed]
20. Mohammadiha, O.; Ghariblu, H. Theoretical analysis of functionally graded thickness tubes under dynamic external inversion loading. *Int. J. Impact Eng.* **2017**, *110*, 162–170. [CrossRef]
21. Zhang, H.; Zhang, X. Crashworthiness performance of conical tubes with nonlinear thickness distribution. *Thin-Walled Struct.* **2016**, *99*, 35–44. [CrossRef]
22. Sun, G.; Xu, F.; Li, G.; Li, Q. Crashing analysis and multiobjective optimization for thin-walled structures with functionally graded thickness. *Int. J. Impact Eng.* **2014**, *64*, 62–74. [CrossRef]
23. Xu, F. Enhancing material efficiency of energy absorbers through graded thickness structures. *Thin-Walled Struct.* **2015**, *97*, 250–265. [CrossRef]
24. Sun, G.; Tian, X.; Fang, J.; Xu, F.; Li, G.; Huang, X. Dynamical bending analysis and optimization design for functionally graded thickness (FGT) tube. *Int. J. Impact Eng.* **2015**, *78*, 128–137. [CrossRef]
25. Zhang, X.; Zhang, H.; Wang, Z. Bending collapse of square tubes with variable thickness. *Int. J. Mech. Sci.* **2016**, *106*, 10–21. [CrossRef]
26. Lu, R.; Liu, X.; Fu, S.; Xu, Z.; Chen, S.; Hu, X.; Liu, L. Experiment and simulation for the crushing of tailor rolled tubes with various geometric parameters. *Int. J. Mech. Sci.* **2018**, *136*, 25–36. [CrossRef]
27. Ying, L.; Zhao, X.; Dai, M.; Zhang, S.; Hu, P. Crashworthiness design of quenched boron steel thin-walled structures with functionally graded strength. *Int. J. Impact Eng.* **2016**, *95*, 72–88. [CrossRef]

28. Deng, Z.; He, C.; Liu, Y.; Kim, K.C. Super-resolution reconstruction of turbulent velocity fields using a generative adversarial network-based artificial intelligence framework. *Phys. Fluids* **2019**, *31*, 125111. [CrossRef]
29. Deng, Z.; He, C.; Liu, Y. Deep neural network-based strategy for optimal sensor placement in data assimilation of turbulent flow. *Phys. Fluids* **2021**, *33*, 025119. [CrossRef]
30. Fukami, K.; Fukagata, K.; Taira, K. Super-resolution reconstruction of turbulent flows with machine learning. *J. Fluid Mech.* **2019**, *870*, 106–120. [CrossRef]
31. Lee, S.; You, D. Prediction of laminar vortex shedding over a cylinder using deep learning. *arXiv* **2017**, arXiv:1712.07854. [CrossRef]
32. Yong, L.; Yang, H.; Yin, Z. PIV-DCNN: Cascaded deep convolutional neural networks for particle image velocity. *Exp. Fluids* **2017**, *58*, 171. [CrossRef]
33. Xie, J.; Wang, S.; Li, Y.; Wang, T.; Yang, J.; Pan, T. A simulated-to-real transfer fault diagnosis method based on prototype clustering subdomain adversarial adaptation network for HST bogie bearing. *IEEE Trans. Instrum. Meas.* **2024**, *73*, 3529313. [CrossRef]
34. Gdaim, S.; Mtibaa, A.; Mimouni, M.F. Artificial neural network-based DTC of an induction machine with experimental implementation on FPGA. *Eng. Appl. Artif. Intell.* **2023**, *121*, 105972. [CrossRef]
35. Liu, J.; Yu, X. Rolling Element Bearing Fault Diagnosis for Complex Equipment based on MFMD and BP Neural Network. *J. Phys. Conf. Ser.* **2021**, *1948*, 012113. [CrossRef]
36. Chen, X.; Zhou, J.; Xiao, J.; Zhang, X.; Xiao, H.; Zhu, W.; Fu, W. Fault diagnosis based on dependent feature vector and probability neural network for rolling element bearings. *Appl. Math. Comput.* **2014**, *247*, 835–847. [CrossRef]
37. Zheng, B.; Li, T.; Qi, H.; Gao, L.; Liu, X.; Yuan, L. Physics-informed machine learning model for computational fracture of quasi-brittle materials without labeled data. *Int. J. Mech. Sci.* **2022**, *223*, 107282. [CrossRef]
38. Zhao, G.; Xu, T.; Fu, X.; Zhao, W.; Wang, L.; Lin, J.; Hu, Y.; Du, L. Machine-learning assisted multiscale modeling strategy for predicting mechanical properties of carbon fiber reinforced polymers. *Compos. Sci. Technol.* **2024**, *248*, 110455. [CrossRef]
39. Xu, T.; Xu, P.; Yang, C.; Li, Z.; Wang, A.; Guo, W. An LSTM-stacked autoencoder multisource response prediction and constraint optimization for scaled expansion tubes. *Appl. Soft Comput.* **2024**, *153*, 111285. [CrossRef]
40. Yang, C.; Meng, K.; Yang, L.; Guo, W.; Xu, P.; Zhou, S. Transfer learning-based crashworthiness prediction for the composite structure of a subway vehicle. *Int. J. Mech. Sci.* **2023**, *255*, 108244. [CrossRef]
41. Guo, W.; Xu, P.; Yang, C.; Guo, J.; Yang, L.; Yao, S. Machine learning-based crashworthiness optimization for the square cone energy-absorbing structure of the subway vehicle. *Struct. Multidiscip. Optim.* **2023**, *66*, 182. [CrossRef]
42. Standardization Administration of China. *GB/T 16865-2013*; Test Pieces and Test Methods for Tensile Testing of Wrought Aluminum, Magnesium and Their Alloys. Standards Press of China: Beijing, China, 2013.
43. Wu, Y.; Zhao, H.; Zhang, C.; Wang, L.; Han, J. Optimization analysis of structure parameters of steam ejector based on CFD and orthogonal test. *Energy* **2018**, *151*, 79–93. [CrossRef]
44. Yao, S.; Yan, K.; Lu, S.; Xu, P. Prediction and application of energy absorption characteristics of thin-walled circular tubes based on dimensional analysis. *Thin-Walled Struct.* **2019**, *130*, 505–519. [CrossRef]

Disclaimer/Publisher's Note: The statements, opinions and data contained in all publications are solely those of the individual author(s) and contributor(s) and not of MDPI and/or the editor(s). MDPI and/or the editor(s) disclaim responsibility for any injury to people or property resulting from any ideas, methods, instructions or products referred to in the content.